Particles II
Access the latest eBook →

11 Advanced Optical Metrology
Particles II

EVIDENT
OLYMPUS
WILEY

Impact on Biological Systems and the Environment

This eBook is dedicated to the research of Professor David Wertheim.
In collaboration with various groups, Professor Wertheim uses confocal microscopy to analyse the impact of different types of particles on human health and the environment, with a focus on human health-hazardous particles detected with solid-state nuclear track detectors (SSNTD). Download for free, today.

EVIDENT
OLYMPUS

WILEY

Self-Assembly of Oriented Antibody-Decorated Metal–Organic Framework Nanocrystals for Active-Targeting Applications

Karen Alt,* Francesco Carraro, Edwina Jap, Mercedes Linares-Moreau, Raffaele Riccò, Marcello Righetto, Marco Bogar, Heinz Amenitsch, Rania A. Hashad, Christian Doonan, Christoph E. Hagemeyer,* and Paolo Falcaro*

Antibody (Ab)-targeted nanoparticles are becoming increasingly important for precision medicine. By controlling the Ab orientation, targeting properties can be enhanced; however, to afford such an ordered configuration, cumbersome chemical functionalization protocols are usually required. This aspect limits the progress of Abs-nanoparticles toward nanomedicine translation. Herein, a novel one-step synthesis of oriented monoclonal Ab-decorated metal–organic framework (MOF) nanocrystals is presented. The crystallization of a zinc-based MOF, $Zn_2(mIM)_2(CO_3)$, from a solution of Zn^{2+} and 2-methylimidazole (mIM), is triggered by the fragment crystallizable (Fc) region of the Ab. This selective growth yields biocomposites with oriented Abs on the MOF nanocrystals (MOF*Ab): the Fc regions are partially inserted within the MOF surface and the antibody-binding regions protrude from the MOF surface toward the target. This ordered configuration imparts antibody–antigen recognition properties to the biocomposite and shows preserved target binding when compared to the parental antibodies. Next, the biosensing performance of the system is tested by loading MOF*Ab with luminescent quantum dots (QD). The targeting efficiency of the QD-containing MOF*Ab is again, fully preserved. The present work represents a simple self-assembly approach for the fabrication of antibody-decorated MOF nanocrystals with broad potential for sensing, diagnostic imaging, and targeted drug delivery.

1. Introduction

Monoclonal antibodies (Abs) are cornerstone biopharmaceuticals that are involved in the treatment of a wide range of conditions, including chronic inflammatory, infectious diseases, cardiovascular diseases, and cancer,[1,2] providing precision medicine not possible with other drugs.[3,4] The efficacy of Abs can be attributed to their capacity to specifically bind molecular components with excellent targeting selectivity.[2,4,5] Furthermore, many of their properties such as antigen-binding specificity, affinity, and cellular internalization can be fine-tuned to improve their clinical utility.[1] To expand their utility, Abs can be combined with functional nanomaterials such as quantum dots (QDs), gold or iron oxide nanoparticles for imaging, sensing, and targeted drug delivery applications.[6] However, when a nanoparticle is decorated with antibodies, the orientation of the protein is typically lost and only part of the binding sites is available for target

K. Alt, E. Jap, R. A. Hashad, C. E. Hagemeyer
Central Clinical School
Australian Centre of Blood Disease
Monash University
Melbourne, Victoria 3004, Australia
E-mail: karen.alt@monash.edu; christoph.hagemeyer@monash.edu

F. Carraro, M. Linares-Moreau, R. Riccò, P. Falcaro
Institute of Physical and Theoretical Chemistry
Graz University of Technology
Graz 8010, Austria
E-mail: paolo.falcaro@tugraz.at

R. Riccò
Department of Industrial Systems Engineering
School of Engineering and Technology
Asian Institute of Technology (AIT)
PO Box 4, Klong Luang, Pathum Thani 12120, Thailand

M. Righetto
Division of Physics and Applied Physics
School of Physical and Mathematical Sciences
Nanyang Technological University
21 Nanyang Link, Singapore 637371, Singapore

M. Bogar, H. Amenitsch
Institute of Inorganic Chemistry
Graz University of Technology
Graz 8010, Austria

R. A. Hashad
Department of Pharmaceutics and Industrial Pharmacy
Faculty of Pharmacy
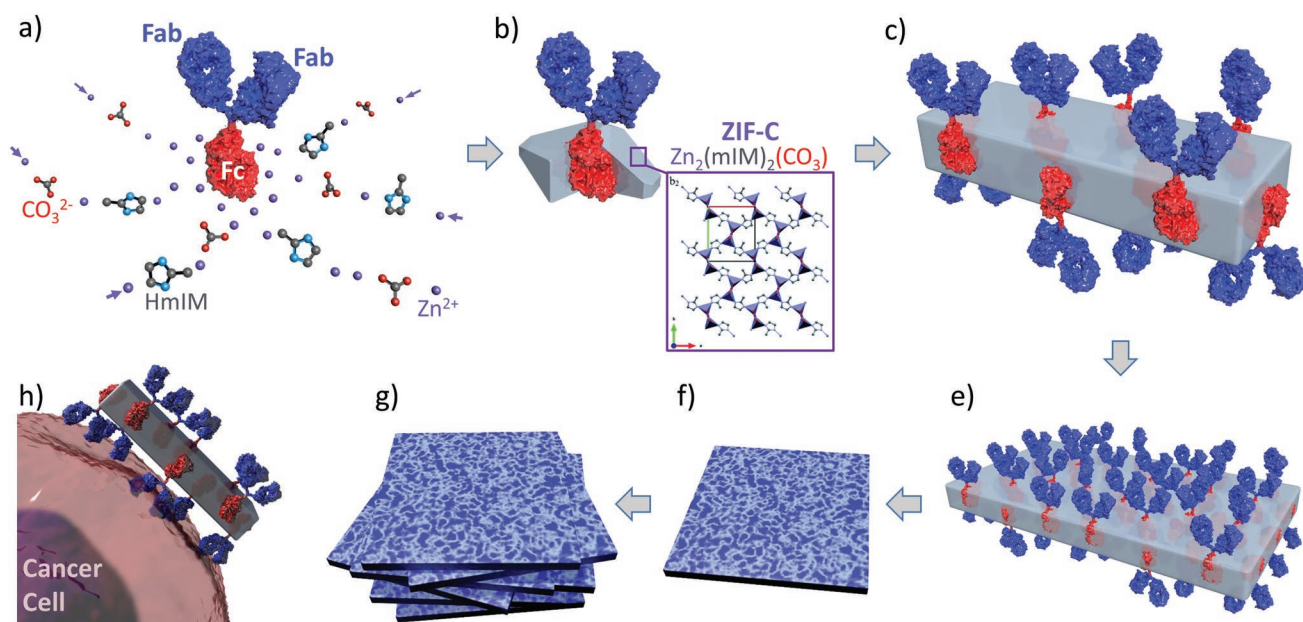Ain Shams University
Cairo 11566, Egypt

ADVANCED
SCIENCE NEWS

www.advancedsciencenews.com

ADVANCED
MATERIALS

www.advmat.de

Figure 1. a) Ab and MOF precursors (Zn^{2+}, HmIM, CO$_3^{2-}$); b) nucleation of ZIF-C around the Fc region (inset shows ZIF-C crystal structure); c–f) growth of plate-like ZIF-C*Ab nanocrystals; g) agglomeration of ZIF-C*Ab nanocrystals; h) proposed targeting application for ZIF-C*Ab.

recognition.[7,8] To enhance the targeting properties of Ab, the protein should ideally be positioned with the fragment crystallizable (Fc) region oriented toward the nanoparticle surface, thereby leaving the fragment antigen-binding (Fab) regions free to target specific antigens.[8] A precise and homogeneous Ab orientation would greatly reduce non-specific tissue interactions and off-target effects in vivo.[7,9] However, precise Ab orientation on particles is made cumbersome by employing chemical protocols (e.g., protein fusion methods) or is limited to specific materials (e.g., gold).[8] Thus, new facile and versatile Ab-directed chemistries will facilitate the use of Ab-targeted particles in modern medicine.[8]

Recently, metal–organic frameworks (MOFs)[10] as nanocrystals have shown promise in biotechnology and biomedical applications.[11–15] MOFs have been combined with Abs, either via encapsulation or site-specific conjugation, for biobanking and immunosensing applications.[11–13,16–22] For instance,[17] to protect the protein from temperature and solvents, Abs were encapsulated within zeolitic imidazolate frameworks (ZIFs[23]). To improve biodetection, Abs were biotinylated on the COOH-rich MOF surface.[24] However, to date, there are no literature reports on the controlled self-assembly of MOFs on selected regions of Abs. Thus, the potential use of MOFs as a simple strategy to achieve precise and homogeneous control of the orientation of Abs remains unexplored. Recently, Maddigan et al. has demonstrated that ZIF-8, constituting Zn^{2+} and 2-methylimidazole, spontaneously self-assembles on proteins with isoelectric points of less than 7;[25] Zn^{2+} concentrate on the surface of biomacromolecules with negatively charged

functional groups (e.g., carboxyl groups), thus promoting the rapid formation of ZIF-8.[25–27] In contrast, the self-assembly of ZIF-8 did not occur in the presence of positively charged proteins.[25] In this context, the surface chemistry and charge distribution of Abs are known to differ significantly between the Fab region and the Fc region: positively charged amino terminal groups of an Ab are located on the Fab region, whereas negatively charged carboxyl and histidine groups are mostly located in the Fc region.[7,28–30] Hence, we hypothesize that the anisotropy of both the shape and surface chemistry of Abs could trigger a spatially controlled crystallization of a Zn-based ZIF predominantly around the Fc region and, thus, afford orientation-controlled insertion of Abs in MOF particles (**Figure 1**).

2. Results and Discussion

To test our hypothesis, two model Abs were employed: (1) humanized monoclonal IgG1 Trastuzumab (α-HER2) that recognizes the extracellular domain of the HER2 receptor (HER2-R), which is overexpressed in different cancer types (e.g., breast, gastric, and ovarian cancer)[31] and (2) commercial human IgG (hIgG) as a control. The respective Abs were added to an aqueous solution of 2-methylimidazole (HmIM) and Zn^{2+} at 37 °C. Upon mixing, the turbidity of the solution rapidly increased, an observation that suggests the biomimetic mineralization of ZIF-8 or other coordination compounds based on Zn cations connected by mIM linkers (Figure S1, Supporting Information).[32] The solid products were collected by centrifugation, washed with water, and examined via X-ray diffraction (XRD). The final products (biocomposites) are referred to as ZIF-C*Ab (Ab = α-HER2 or hIgG). The diffraction patterns of ZIF-C*Abs were assigned to ZIF-CO$_3$-1[33] (i.e., ZIF-C, CCDC 1032088) (Figures 1b and 2a; Figure S2, Supporting Information).

C. Doonan
School of Physical Sciences
Faculty of Sciences
University of Adelaide
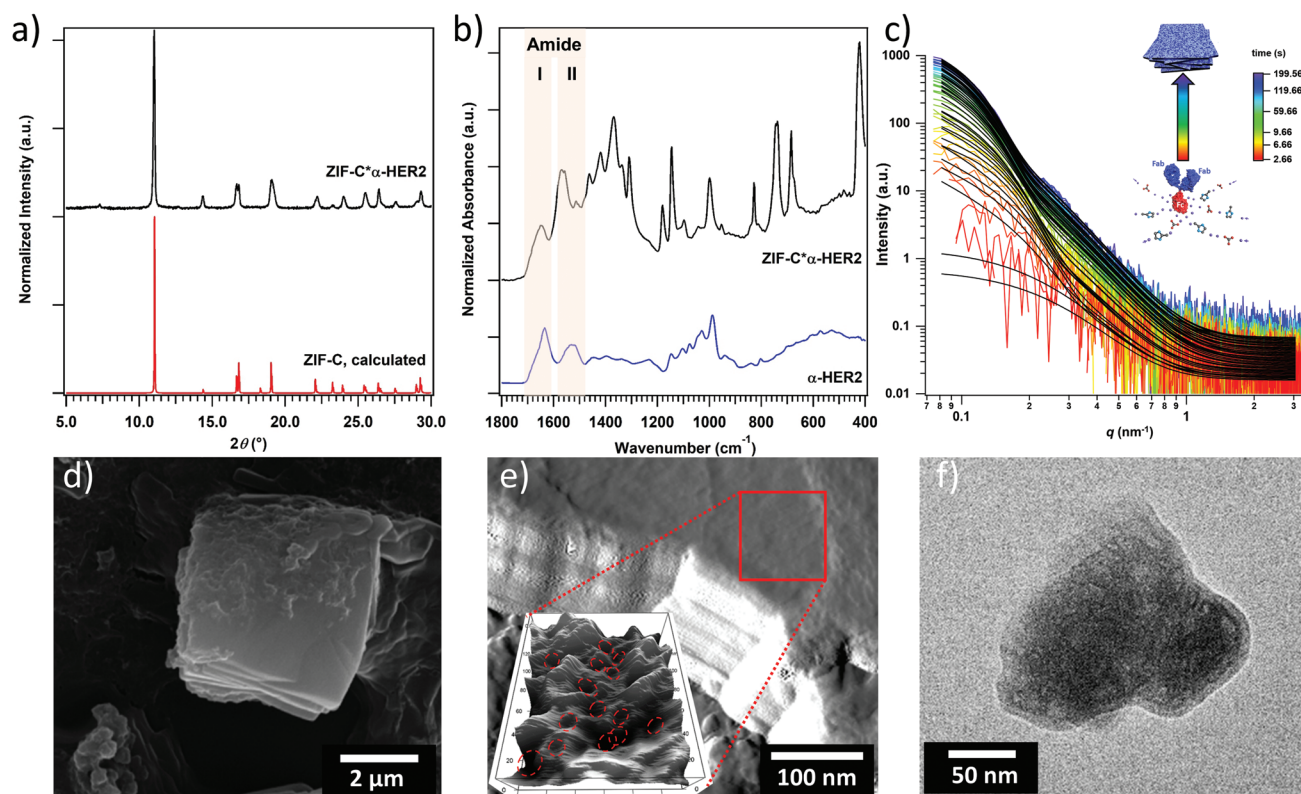Adelaide, South Australia 5005, Australia

**ADVANCED
SCIENCE NEWS**

www.advancedsciencenews.com

**ADVANCED
MATERIALS**

www.advmat.de

Figure 2. a) XRD patterns of ZIF-C*α-HER2 and calculated ZIF-C. b) FTIR spectra of α-HER2 and ZIF-C*α-HER2. c) Time-resolved SAXS patterns of the nucleation and growth of ZIF-C*α-HER2. d) SEM image of ZIF-C*α-HER2. e) AFM amplitude image of pyrolyzed ZIF-C*α-HER2; the inset shows a 3D topography of a 100×100 nm^2 region with cavities. f) TEM image of pyrolyzed ZIF-C*α-HER2.

ZIF-C is a dense $Zn_2(mIM)_2(CO_3)$ phase that was obtained when bovine serum albumin and insulin were used as seeding agents in an aqueous solution of HmIM and Zn^{2+}.[34,35] The source of CO_3^{2-} anions used for the construction of the framework is atmospheric CO_2. When compared with $Zn(mIM)_2$ ZIF phases (e.g., amorphous, diamondoid, and sodalite ZIF-8), ZIF-C has distinct chemico-physical and functional properties.[34,35] The ZIF-C*Ab biocomposites were examined by Fourier transform infrared (FTIR) spectroscopy (**Figure** 2b; Figure S3, Supporting Information). The spectra featured vibrational modes assigned to ZIF-C[33,34,36,37] (e.g Zn—N stretching mode at 424 cm^{-1}, CO_3^{2-} bending mode at 828 cm^{-1}, and asymmetric stretching modes of CO_3^{2-} at 1575 and 1375 cm^{-1}) and to the peptide backbone of the antibodies, amide I (1600–1710 cm^{-1}) and amide II (1480–1595 cm^{-1}) bands,[38] thus confirming the successful integration of the Abs within ZIF-C. The immobilization efficiency of Ab α-HER2 onto ZIF-C was quantitatively determined (100%) via bicinchoninic acid assay of the supernatant (Figure S4, Supporting Information).

The morphology of the biocomposites ZIF-C*α-HER2 and ZIF-C*hIgG was examined by scanning electron microscopy (SEM), transmission electron microscopy (TEM), and atomic force microscopy (AFM). SEM images (Figure 2d; Figure S5, Supporting Information) show the presence of two populations of particles: micrometer-sized lamellar particles and clusters of smaller particles. ZIF-C*α-HER2 was selected as a model system for an in-depth investigation of the biocomposite

morphology. TEM analysis confirmed the lamellar structure of ZIF-C*α-HER2, constituting clusters of plates (0.1–6 μm) made of lower and higher contrast lamellae inclusion (plate perpendicular and parallel to the electron beam, respectively). The estimated thickness of the lamellae was 2–3 nm with an average lateral dimension of 25 nm (Figure S6, Supporting Information).

To study the formation of the ZIF-C*α-HER2 particles, time-resolved small-angle X-ray scattering (SAXS) experiments, using a stopped-flow cell (Figure S7, Supporting Information) setup,[39] were performed in the presence and absence of the Ab in the MOF precursor solution. The formation of the biocomposite occurred over a time scale of seconds, as seen in the time-resolved SAXS patterns and calculated Porod invariant in Figure 2c; Figure S8, Supporting Information. Modeling of the SAXS curves revealed that near-spherical particles of ≈10 nm rapidly form, followed by a transition to plate-like structures after 3.6 s upon mixing of the reagents (Figure 1a–f). As the reaction proceeds, the plate-like structures aggregate to form layered superstructures in solution (Figure 1f,g). These modeling results confirm the topological information obtained from the microscopy analysis discussed earlier. Fitting of the SAXS pattern of the dry particles revealed the presence of cavities with an average size of 3 nm on the particles (Figure S9, Supporting Information). The size of the cavities of the MOF particles is comparable with the size of the Fc region.[40] Conversely, in the absence of an Ab, a slow 3D growth of

ADVANCED
SCIENCE NEWS
www.advancedsciencenews.com

ADVANCED
MATERIALS
www.advmat.de

spherical MOF particles of <100 nm was obtained (Figure S10, Supporting Information). From these in situ synchrotron SAXS data, we conclude that Ab triggers the formation of the MOF, and the ZIF-C*α-HER2 biocomposite is formed via biomimetic mineralization. More importantly, the data suggest that the Fc region of the Abs is embedded in ZIF-C.

The influence of the different constituent fractions of the antibody (i.e., Fc, Fab, F(ab')2, sialylglycopeptide (SGP), and sialylglycan (SG), Figure S11, Supporting Information) on the MOF formation was examined by in situ SAXS analysis. Rapid formation of MOF particles with the same plate-like morphology as that obtained with Ab α-HER2 as a whole was only observed in the presence of the Fc component (Figure S12, Supporting Information). In the presence of the other components, particle formation was comparable with that obtained in the absence of an Ab (Table S1 and Figures S13–S16, Supporting Information). These results confirmed that the Fc region of the Ab is the only part responsible for the formation of ZIF-C with a plate-like structure.

To further investigate the immobilization geometry of the Ab in the MOF lamellae, ZIF-C*α-HER2 was pyrolyzed at 325 °C following a protocol previously used for the localization of proteins in ZIF biocomposites.[41] As observed from Figures S17 and S18, Supporting Information, the crystallinity of ZIF-C*α-HER2 and the overall morphology of the nanocrystals were preserved after pyrolysis. TEM analysis revealed the presence of pores with a diameter of 10–15 nm (Figure 2f). AFM confirmed that pyrolyzed ZIF-C*α-HER2 were constituted of plates with a typical thickness of 3–5 nm (Figures S19 and S20, Supporting Information). AFM analysis of the surface of the pyrolyzed ZIF-C crystals also revealed the presence of cavities with a width of 11 ± 3 nm (Figure 2e; Figures S19–S21, Supporting Information), consistent with the TEM results. These cavities were formed upon thermal decomposition of the Fc regions in ZIF-C, while the thickness of the plates (3–5 nm) suggests that the F(ab')2 fraction is exposed from the plate with perpendicular orientation. Thus, these structural investigations support the hypothesis that preferential nucleation and growth of ZIF-C can occur on the Fc region. The different charge distribution in the antibody regions (i.e., the Fc part that is more negatively charged than the Fab part)[42,43] can explain the accumulation of Zn^{2+} in the Fc region.[25] This results in the selective nucleation of ZIF-C in the Fc region either as part of a complete antibody system or as an isolated fragment (see Figures S8 and S12, Supporting Information). The preferential localization of amino-terminal groups in the Fab region[7] could explain the negligible biomimetic-mineralization properties of this fragment, either as part of a complete antibody system or as an isolated fragment (see Figures S10 and S13, Supporting Information).[25] As a result, a MOF biocomposite particle with a precise insertion of antibodies, available for targeting applications, was obtained. Moreover, the data suggest the versatility of the present synthesis strategy in terms of its applicability to a range of antibodies considering that the Fc region is highly preserved between different Abs, whereas the Fab region varies highly depending on the targeted antigens.

The accessibility of the F(ab')2 components in ZIF-C*α-HER2, and thus the orientation of Ab, was studied for active cell targeting. α-HER2 was pre-labeled with an N-hydroxysuccinimide ester-activated Alexa Fluor 488 (Al488) fluorophore, and thereafter referred to as α-fHER2. To examine the potential use of ZIF-C*fAb (Ab = α-fHER2 or fhIgG) for cellular delivery, the cellular internalization process of ZIF-C*α-fHER2 was assessed by immunofluorescence assays. HER2-R+ (SKOV-3) cells were incubated with either ZIF-C*α-fHER2 or ZIF-C*fhIgG at 37 °C and stained for DNA (4',6-diamidino-2-phenylindole, DAPI) with or without the cell membrane dye Wheat Germ Agglutinin, Alexa Fluor 647 (**Figure 3**e; Figures S22 and S23, Supporting Information). The ZIF-C*α-fHER2 biocomposite was efficiently internalized by the HER2-R+ cells as opposed to the HER2-R− (MDA-MB-231) cells, which showed only minimal binding. Control ZIF-C*fhIgG showed no significant internalization by HER2-R+ cells (Figure 3e; Figures S22 and S23, Supporting Information), further confirming the targeting properties of the biocomposite.

To broaden the scope of the present ZIF-C*Ab system in other applications, the encapsulation of other materials such as QDs[44] during the synthesis of ZIF-C*fAb was examined to generate fluorescent particles for potential diagnostic applications. The XRD patterns and FTIR vibrational modes obtained for the QD@ZIF-C*Ab biocomposites (Figure S24, Supporting Information) were identical to those of ZIF-C*Ab (Figure 2a,b). Energy-dispersive X-ray spectroscopy and TEM analyses showed that the QDs were encapsulated within the biocomposite (Figure 3j; Figures S25 and S26, Supporting Information), thus confirming the successful preparation of QD@ZIF-C*Ab (Figure 3g–j). To quantitatively evaluate the targeting capabilities and the structural integrity of the biocomposite QD@ZIF-C*fAb, the biocomposite was incubated with HER2-R+ or HER2-R− cell lines and the co-localization of the QD signal and the labeled Ab signal was determined (Figure 3k). QD@ZIF-C*α-fHER2 demonstrated significant binding to HER2-R+ cells than to HER2-R- cells with a mean fluorescence intensity (MFI) of 94.1% over 14% ($p \leq 0.0001$)(Figure 3l). In contrast, minimal binding between control QD@ZIF-C*fhIgG and SKOV-3 cells or between QD@ZIF-C*α-fHER2 and HER2-R− cells was observed (Figure 3k,l), further confirming the specificity of the biocomposite. Additional confirmation was achieved by blocking the cell antigen binding sites with 50 µg of the parental antibody 30 min prior to the biocomposite incubation resulting in a significant decrease of QD@ZIF-C*α-fHER2 binding to its target ($p \leq 0.0001$)(Figure 3l).

3. Conclusion

We have demonstrated that the surface chemistry of biomacromolecules can be used for the spatially selective crystallization of MOFs. Specifically, Abs were employed to induce the growth of a zinc-based MOF (ZIF-C) on the Fc region of Abs via a one-step approach. The localized growth of ZIF-C on the Fc region resulted in a MOF biocomposite (ZIF-C*Ab) with the Fab regions protruded from the MOF nanocrystal surface and free to target the selected antigen. The applicability of this protocol to biosensing was demonstrated by the successful encapsulation of QDs into ZIF-C*Ab and the measured targeting performance. This simple synthetic approach has the potential
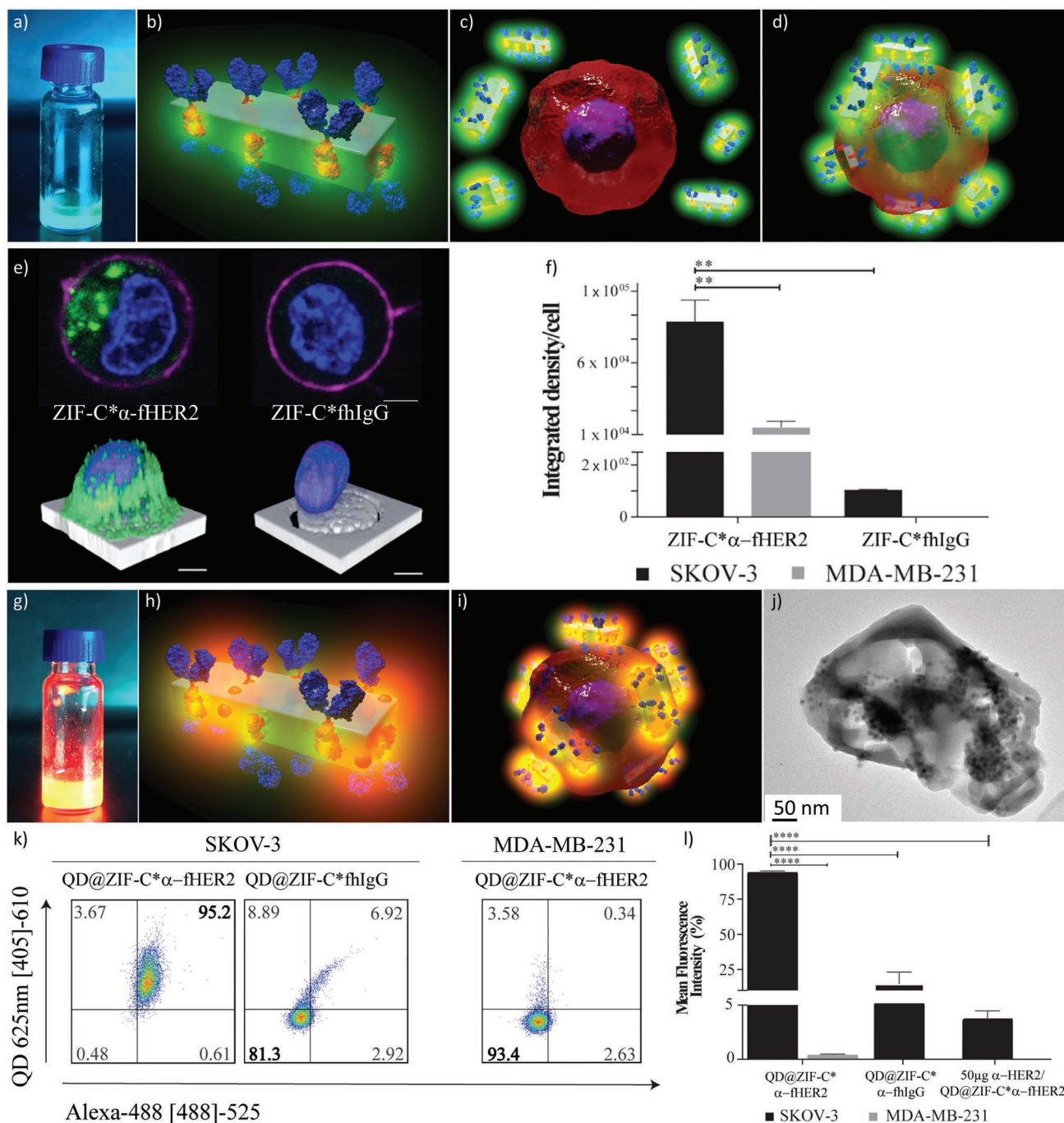
Figure 3. a) Photograph of a ZIF-C*α-fHER2 solution under UV light. b–d) Schematic illustrations of ZIF-C*α-fHER2 with Ab Fc region (red) and Ab antigen binding site (blue) (b) and binding of ZIF-C*α-fHER2 to its target cell (nucleus = purple, cell membrane = red) (c,d). e) 2D and 3D confocal microscopy images of ZIF-C*fAb internalization (Ab = α-fHER2 or fhIgG, green). SKOV-3 (HER2-R+) cells post 30 min incubation at 37 °C with either ZIF-C*fHER2 (left) or ZIF-C*fIgG (right) presented in either 2D (top) or 3D (bottom). Cell nuclei were stained with 4′,6-diamidino-2-phenylindole (blue) and cell membranes stained with Wheat Germ Agglutinin, Alexa Fluor 647 in the 2D data set (pink/bottom). Scale bar: 5 µm. The full z-stack is shown in Figure S22, Supporting Information; additional 3D data is shown in Figure S23, Supporting Information. f) Statistical analysis of the immunofluorescence assay (e), wherein the mean of the ZIF-C*fAb as positive signal (FITC) in the cell was measured. g) Photograph of a QD@ZIF-C*α-fHER2 solution under UV light. h,i) Schematic illustrations of QD@ZIF-C*α-fHER2 (h) and binding of QD@ZIF-C*α-fHER2 to its target cell (i). j) TEM image of QD@ZIF-C*α-fHER2. Co-localization of Alexa-488 fluorochrome and Qd 624 nm. k) Representative dot plots of the ZIF-C*fAb binding efficiency to different cell lines. ZIF-C*fHER2 and QD@ZIF-C*fHER2 to SKOV-3 are shown. ZIF-C*fhIgG was used as a control for binding to SKOV-3 cells and ZIF-C*α-fHER2 was used as a control for binding to MDA-MB-231 cells. The displayed values represent fluorescence intensity in percentage. l) Flow cytometry analysis based on the co-localization of QD 625 nm and Al488 fluorescence positive signal. Statistical analysis was performed using two-way analysis of variance (ANOVA) followed by a multiple comparison test (Tukey test) (± standard error of the mean (S.E.M.)) ($n = 3$); with **$p \leq 0.05$, ****$p \leq 0.001$ considered as statistically significant.

to be extended from antibody-based sensing to diagnostic and therapeutic applications.

Conflict of Interest

The authors declare no conflict of interest.

Data Availability Statement

The data that support the findings of this study are available from the corresponding author upon reasonable request.

[1] P. J. Carter, *Nat. Rev. Immunol.* **2006**, *6*, 343.
[2] P. J. Carter, G. A. Lazar, *Nat. Rev. Drug Discovery* **2017**, *17*, 197.
[3] B. Conte, A. Fabi, F. Poggio, E. Blondeaux, C. Dellepiane, A. D'Alonzo, G. Buono, G. Arpino, V. Magri, G. Naso, D. Presti, S. Mura, A. Fontana, F. Cognetti, C. Molinelli, S. Pastorino, C. Bighin, I. Miglietta, F. Boccardo, M. Lambertini, L. D. Mastro, G. I. M. (GIM) study group, *Clin. Breast Cancer* **2020**, *20*, e181.
[4] N. Gravbrot, K. Gilbert-Gard, P. Mehta, Y. Ghotmi, M. Banerjee, C. Mazis, S. Sundararajan, *Antibodies* **2019**, *8*, 51.
[5] C. Achille, C. Parra-Cabrera, R. Dochy, H. Ordutowski, A. Piovesan, P. Piron, L. V. Looy, S. Kushwaha, D. Reynaerts, P. Verboven, B. Nicolaï, J. Lammertyn, D. Spasic, R. Ameloot, *Adv. Mater.* **2021**, *33*, 2008712.
[6] D. A. Richards, A. Maruani, V. Chudasama, *Chem. Sci.* **2017**, *8*, 63.
[7] M. Tonigold, J. Simon, D. Estupiñán, M. Kokkinopoulou, J. Reinholz, U. Kintzel, A. Kaltbeitzel, P. Renz, M. P. Domogalla, K. Steinbrink, I. Lieberwirth, D. Crespy, K. Landfester, V. Mailänder, *Nat. Nanotechnol.* **2018**, *13*, 862.
[8] A. K. Trilling, J. Beekwilder, H. Zuilhof, *Analyst* **2013**, *138*, 1619.
[9] R. S. Riley, C. H. June, R. Langer, M. J. Mitchell, *Nat. Rev. Drug Discovery* **2019**, *18*, 175.
[10] H.-C. Zhou, J. R. Long, O. M. Yaghi, *Chem. Rev.* **2012**, *112*, 673.
[11] A. C. McKinlay, R. E. Morris, P. Horcajada, G. Férey, R. Gref, P. Couvreur, C. Serre, *Angew. Chem., Int. Ed.* **2010**, *49*, 6260.
[12] C. Doonan, R. Riccò, K. Liang, D. Bradshaw, P. Falcaro, *Acc. Chem. Res.* **2017**, *50*, 1423.
[13] H.-X. Zhao, Q. Zou, S.-K. Sun, C. Yu, X. Zhang, R.-J. Li, Y.-Y. Fu, *Chem. Sci.* **2016**, *7*, 5294.
[14] M. A. Luzuriaga, R. P. Welch, M. Dharmarwardana, C. E. Benjamin, S. Li, A. Shahrivarkevishahi, S. Popal, L. H. Tuong, C. T. Creswell, J. J. Gassensmith, *ACS Appl. Mater. Interfaces* **2019**, *11*, 9740.
[15] Y. Li, K. Zhang, P. Liu, M. Chen, Y. Zhong, Q. Ye, M. Q. Wei, H. Zhao, Z. Tang, *Adv. Mater.* **2019**, *31*, 1901570.
[16] S. K. Bhardwaj, N. Bhardwaj, G. C. Mohanta, P. Kumar, A. L. Sharma, K.-H. Kim, A. Deep, *ACS Appl. Mater. Interfaces* **2015**, *7*, 26124.
[17] Y. Feng, H. Wang, S. Zhang, Y. Zhao, J. Gao, Y. Zheng, P. Zhao, Z. Zhang, M. J. Zaworotko, P. Cheng, S. Ma, Y. Chen, *Adv. Mater.* **2019**, *31*, 1805148.
[18] C. Wang, J. Gao, H. Tan, *ACS Appl. Mater. Interfaces* **2018**, *10*, 25113.
[19] C. Wang, S. Tadepalli, J. Luan, K. Liu, J. J. Morrissey, E. D. Kharasch, R. R. Naik, S. Singamaneni, *Adv. Mater.* **2017**, *29*, 1604433.
[20] L. Kang, S. Smith, C. Wang, *J. Colloid Interface Sci.* **2021**, *588*, 101.
[21] Y. Li, H. Guo, Z. Yin, K. Lyle, L. Tian, *ACS Appl. Mater. Interfaces* **2021**, *13*, 5564.
[22] Q. Cheng, F. Gao, W.-Y. Yu, M.-Z. Zou, X.-L. Ding, M.-J. Li, S.-X. Cheng, X.-Z. Zhang, *Adv. Funct. Mater.* **2020**, *30*, 2000335.
[23] H. Hayashi, A. P. Côté, H. Furukawa, M. O'Keeffe, O. M. Yaghi, *Nat. Mater.* **2007**, *6*, 501.
[24] X. Qi, Z. Chang, D. Zhang, K. J. Binder, S. Shen, Y. Y. S. Huang, Y. Bai, A. E. H. Wheatley, H. Liu, *Chem. Mater.* **2017**, *29*, 8052.
[25] N. K. Maddigan, A. Tarzia, D. M. Huang, C. J. Sumby, S. G. Bell, P. Falcaro, C. J. Doonan, *Chem. Sci.* **2018**, *9*, 4217.
[26] E. Astria, M. Thonhofer, R. Ricco, W. Liang, A. Chemelli, A. Tarzia, K. Alt, C. E. Hagemeyer, J. Rattenberger, H. Schroettner, T. Wrodnigg, H. Amenitsch, D. M. Huang, C. J. Doonan, P. Falcaro, *Mater. Horiz.* **2019**, *6*, 969.
[27] G. Chen, X. Kou, S. Huang, L. Tong, Y. Shen, W. Zhu, F. Zhu, G. Ouyang, *Angew. Chem., Int. Ed.* **2020**, *59*, 2867.
[28] C. A. Janeway, P. Travers, M. Walport, M. J. Shlomchik, *Immunobiology: The Immune System in Health and Disease*, 5th ed., Garland Science, New York **2001**.
[29] A. Tiwari, A. N. Nordin, *Advanced Biomaterials and Biodevices*, Scrivener Publishing, Beverly, MA, USA **2018**.
[30] W. Zhang, Q. A. Besford, A. J. Christofferson, P. Charchar, J. J. Richardson, A. Elbourne, K. Kempe, C. E. Hagemeyer, M. R. Field, C. F. McConville, I. Yarovsky, F. Caruso, *Nano Lett.* **2020**, *20*, 2660.
[31] C. A. Hudis, *N. Engl. J. Med.* **2007**, *357*, 39.
[32] K. Liang, R. Ricco, C. M. Doherty, M. J. Styles, S. Bell, N. Kirby, S. Mudie, D. Haylock, A. J. Hill, C. J. Doonan, P. Falcaro, *Nat. Commun.* **2015**, *6*, 7240.
[33] S. A. Basnayake, J. Su, X. Zou, K. J. Balkus, *Inorg. Chem.* **2015**, *54*, 1816.
[34] F. Carraro, M. de, J. Velásquez-Hernández, E. Astria, W. Liang, L. Twight, C. Parise, M. Ge, Z. Huang, R. Ricco, X. Zou, L. Villanova, C. O. Kappe, C. Doonan, P. Falcaro, *Chem. Sci.* **2020**, *11*, 3397.

**ADVANCED
SCIENCE NEWS**

www.advancedsciencenews.com

**ADVANCED
MATERIALS**

www.advmat.de

[35] J. T. Ryman, B. Meibohm, *CPT: Pharmacometrics Syst. Pharmacol.* **2017**, *6*, 576.

[36] Y. Hu, H. Kazemian, S. Rohani, Y. Huang, Y. Song, *Chem. Commun.* **2011**, *47*, 12694.

[37] M. He, J. Yao, Q. Liu, K. Wang, F. Chen, H. Wang, *Microporous Mesoporous Mater.* **2014**, *184*, 55.

[38] S.-J. Han, P. Rathinaraj, S.-Y. Park, Y. K. Kim, J. H. Lee, I.-K. Kang, J.-S. Moon, J. G. Winiarz, *Biomed Res. Int.* **2014**, *2014*, 954307.

[39] J. Cravillon, C. A. Schröder, R. Nayuk, J. Gummel, K. Huber, M. Wiebcke, *Angew. Chem., Int. Ed.* **2011**, *50*, 8067.

[40] Y. H. Tan, M. Liu, B. Nolting, J. G. Go, J. Gervay-Hague, G. Liu, *ACS Nano* **2008**, *2*, 2374.

[41] F. Lyu, Y. Zhang, R. N. Zare, J. Ge, Z. Liu, *Nano Lett.* **2014**, *14*, 5761.

[42] D. Yang, R. Kroe-Barrett, S. Singh, T. Laue, *Antibodies* **2019**, *8*, 24.

[43] J. Arora, Y. Hu, R. Esfandiary, H. A. Sathish, S. M. Bishop, S. B. Joshi, C. R. Middaugh, D. B. Volkin, D. D. Weis, *mAbs* **2016**, *8*, 1561.

[44] B. Dubertret, P. Skourides, D. J. Norris, V. Noireaux, A. H. Brivanlou, A. Libchaber, *Science* **2002**, *298*, 1759.

2106607 (7 of 7)